



# Nanoparticle surfactants for kinetically arrested photoactive assemblies to track light-induced electron transfer

Kamil Sokołowski<sup>1,2,7</sup>, Junyang Huang<sup>3,7</sup>, Tamás Földes<sup>4,6</sup>, Jade A. McCune<sup>1</sup>, David D. Xu<sup>1</sup>, Bart de Nijs<sup>3</sup>, Rohit Chikkaraddy<sup>3</sup>, Sean M. Collins<sup>5</sup>, Edina Rosta<sup>4,6</sup>, Jeremy J. Baumberg<sup>3</sup> and Oren A. Scherman<sup>1</sup>✉

**Nature controls the assembly of complex architectures through self-limiting processes; however, few artificial strategies to mimic these processes have been reported to date. Here we demonstrate a system comprising two types of nanocrystal (NC), where the self-limiting assembly of one NC component controls the aggregation of the other. Our strategy uses semiconducting InP/ZnS core-shell NCs (3 nm) as effective assembly modulators and functional nanoparticle surfactants in cucurbit[*n*] uril-triggered aggregation of AuNCs (5–60 nm), allowing the rapid formation (within seconds) of colloidal stable hybrid aggregates. The resultant assemblies efficiently harvest light within the semiconductor substructures, inducing out-of-equilibrium electron transfer processes, which can now be simultaneously monitored through the incorporated surface-enhanced Raman spectroscopy-active plasmonic compartments. Spatial confinement of electron mediators (for example, methyl viologen (MV<sup>2+</sup>)) within the hybrids enables the direct observation of photogenerated radical species as well as molecular recognition in real time, providing experimental evidence for the formation of elusive  $\sigma$ -(MV<sup>+</sup>)<sub>2</sub> dimeric species. This approach paves the way for widespread use of analogous hybrids for the long-term real-time tracking of interfacial charge transfer processes, such as the light-driven generation of radicals and catalysis with operando spectroscopies under irreversible conditions.**

Colloidally integrated hybrid nanostructures comprising semiconductor and metal components are of great interest in materials development and application in next-generation (photo)catalysis, optoelectronics and nanophotonics, as well as drug delivery, sensing and nanotheranostics<sup>1–3</sup>. To date, methods leading to assemblies based on nanocrystals (NCs) have relied on the aggregation of constituent particles by attractive van der Waals<sup>4</sup> and anisotropic interactions<sup>5</sup>, electrostatic forces<sup>6</sup>, multitopic ligands<sup>7</sup>, biotin–streptavidin systems<sup>8</sup> or DNA-based junctions<sup>9</sup>. These self-organization processes usually require time-consuming evaporation of solvent or use of an antisolvent<sup>4,6</sup>, elevated temperature<sup>4–6,9</sup> and/or NC surface modification<sup>9</sup>. Moreover, once induced, self-assembly usually continues until the nanoparticulate components are consumed, yielding crystals<sup>4,6,7</sup>, complex solids<sup>4</sup> or amorphous precipitates<sup>4</sup>. Consequently, colloidal stabilization of NC aggregates remains challenging and—for aqueous systems—particularly rare<sup>10–12</sup>.

A straightforward, yet unexplored, approach to control colloidal aggregates is through self-limiting assembly processes, where NC components can also play an active role in stabilizing the resultant assemblies<sup>5,13</sup>. These processes consist of the assembly of NCs either solely<sup>3</sup> or supported by protein templates<sup>14</sup> and require temperature and/or pH modulation to trigger self-organization (Fig. 1a,b)<sup>5,15</sup>. The resulting structures comprise one type of NC aggregate; however, hybrids comprising two or more types have not yet been achieved through self-limiting processes. Only recently has this approach

been utilized to fabricate precisely, spatially organized NCs yielding discrete clusters with molecule-like symmetry (Fig. 1b)<sup>16,17</sup>.

Employing the self-limiting assembly of one NC component to inherently control the unlimited aggregation of another (Fig. 1c) is conceptually different from currently reported systems. It would unveil a convenient method for the facile hybridization of NC constituents as well as the kinetic entrapment of elusive aggregate phases<sup>18</sup>. Here we introduce a strategy for the kinetic arrest and stabilization of metastable plasmonic assemblies within photoactive NC arrays through interfacial self-limiting aggregation (ISLA). This new hybridization strategy relies on the molecular-glue-mediated self-limiting assembly of semiconductor NCs at the interfaces of growing plasmonic NC aggregates. Semiconductor InP/ZnS core-shell NCs rapidly (within seconds) modulate cucurbit[*n*]uril (CB[*n*]; *n* = 5–8)-triggered assembly of AuNCs (refs. 19–21), passivating their interfaces and stabilizing their kinetically arrested states. Our room-temperature approach results in colloidal stable hybrids formed either from two types of aggregate (Fig. 2a; pathway (1)) or well-dispersed metal NCs entrapped within semiconductor NC arrays (Fig. 2a; pathway (2)). The resulting hybrid assembly is permeable and able to efficiently absorb small molecules (such as electron mediators (EMs); Fig. 2c) on account of the rigid CB[*n*] junction motifs that act as both molecular-glue and subnanometre separators, providing readily accessible interstitial spaces. As the hybrids consist of both photocatalytic and surface-enhanced Raman spectroscopy (SERS)-active components, they yield attractive opportunities for

<sup>1</sup>Melville Laboratory for Polymer Synthesis, Yusuf Hamied Department of Chemistry, University of Cambridge, Cambridge, UK. <sup>2</sup>Institute of Physical Chemistry, Polish Academy of Science, Warsaw, Poland. <sup>3</sup>NanoPhotonics Centre, Cavendish Laboratory, University of Cambridge, Cambridge, UK.

<sup>4</sup>Department of Chemistry, King's College London, London, UK. <sup>5</sup>Department of Materials Science and Metallurgy, University of Cambridge, Cambridge, UK. <sup>6</sup>Department of Physics and Astronomy, University College London, Gower Street, UK. <sup>7</sup>These authors contributed equally: Kamil Sokołowski, Junyang Huang. ✉e-mail: [oas23@cam.ac.uk](mailto:oas23@cam.ac.uk)

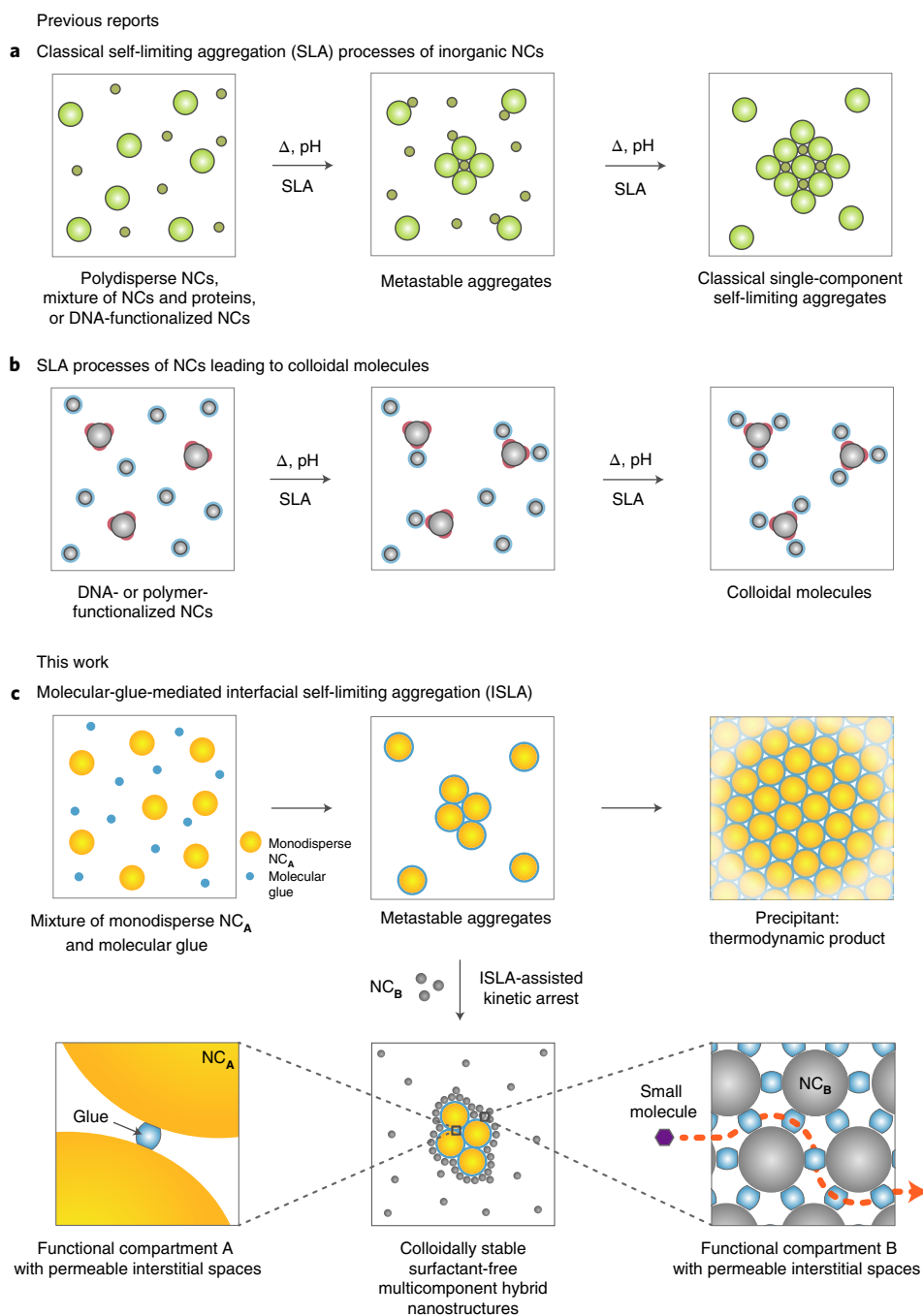


**Fig. 1 | Self-limiting assembly processes.** **a, b**, Previous reports.  $\Delta$ , pH indicates heat and/or pH modifications used to trigger transformations. **c**, The novel strategy described here. NC<sub>A</sub> and NC<sub>B</sub> are two types of nanocrystals, where NC<sub>A</sub> form initial (primary) aggregates and NC<sub>B</sub> act as functional nanoparticle surfactants to kinetically trap and stabilize emerging NC<sub>A</sub> aggregates.

the in situ tracking of light-driven electron transfer processes confined at NC interfaces.

**Molecular-glue-mediated self-limiting aggregation of InP/ZnS NCs.** InP/ZnS core-shell NCs (**1**; Fig. 2b) stabilized by negatively charged 3-mercaptopropionate species (3-MPA) were selected as a model chalcogenide to probe interactions with CB[n] macrocycles<sup>22,23</sup>. To explore the kinetic entrapment of plasmonic aggregates, we employed AuNCs (**2a** and **2b**; Fig. 1b) stabilized by citrate, which exhibit well-established optical properties and strong binding affinity to CB[n] species<sup>19–21</sup>. The NCs were monodisperse

with inorganic core diameters of  $2.8 \pm 0.5$  nm (**1**),  $12.0 \pm 0.9$  nm (**2a**) and  $60.0 \pm 2.4$  nm (**2b**) and average hydrodynamic diameters ( $D_h$ ) of  $3.3 \pm 0.7$  nm (**1**),  $13.3 \pm 3.1$  nm (**2a**) and  $62.3 \pm 22.9$  nm (**2b**) (Supplementary Figs. 1–3). All NCs were water-soluble, stable and did not aggregate when kept either in separate aqueous solutions or when mixed together in various ratios.

To investigate if CB[7] exhibits affinity to the interfaces of **1** NCs, aqueous solutions of **1** and CB[7] are mixed together in various ratios (Fig. 3a). A highly luminescent flocculent material precipitates from the solution in a few seconds when the ratio of CB[7]:**1** ( $\chi$ ) is 100 (Supplementary Fig. 4). The isolated solids, **1**:CB[7], consist of NCs

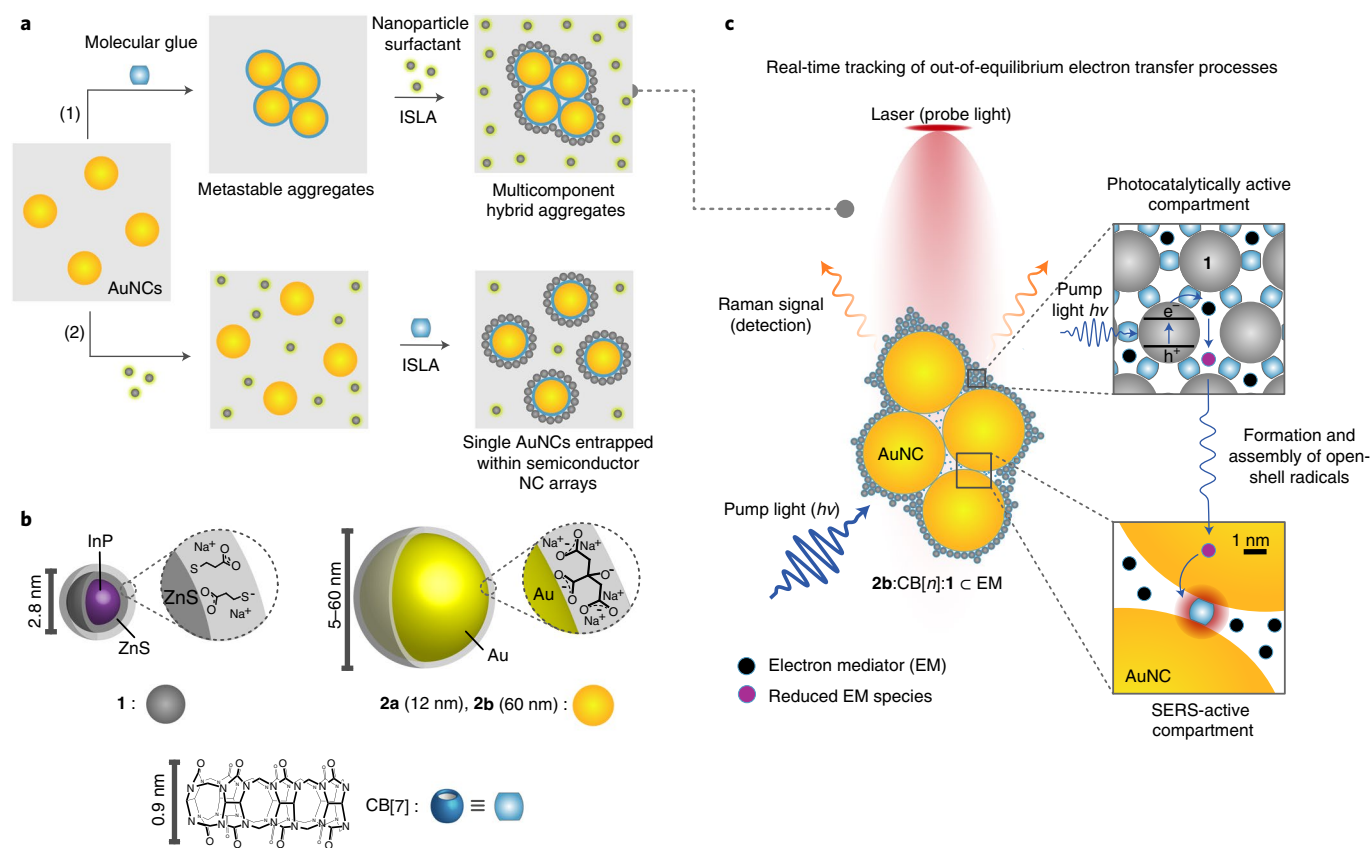


**Fig. 2 | Schematic of ISLA-assisted self-assembly processes of semiconductor/metal hybrids.** **a**, ISLA leading to the (1) kinetic arrest of metastable plasmonic NC assemblies with a functional colloidal surfactant and (2) entrapment of single AuNCs within semiconductor NC arrays. **b**, Building blocks used in the studies here: InP/ZnS core-shell NC (left), AuNC (right) and cucurbit[7]uril molecular glue (bottom). **c**, Schematic of bifunctional colloidal stable hybrid aggregates, emphasizing their photocatalytic and SERS activity for the real-time tracking of interfacial electron transfer. These hybrids are chemically simple (since only the functional NCs and molecular junction are involved) and permeable towards additional species in solution for subsequent chemistry (avoiding thick organic surfactant layers or inorganic silica shells).

of **1** with CB[7] and 3-MPA in an approximate ratio of  $1_{\mathbf{1}}:20_{\text{CB}[7]}:40_{\text{3-MPA}}$ , as estimated by NMR and infrared spectroscopies along with elemental analysis (Supplementary Figs. 7–9). Electron microscopy (transmission electron microscopy (TEM) and scanning transmission electron microscopy (STEM)) data reveal a loosely packed open network structure of **1**:CB[7] precipitates (Supplementary Fig. 5)<sup>24</sup>. Stable colloids of **1**:CB[7] (several weeks) are observed when the CB[7]:**1** ratio  $N_{\text{CB}[7]}/N_{\mathbf{1}} = \chi < 18$  (where  $N_{\text{CB}[7]}$  is the number of CB[7] macrocycles and  $N_{\mathbf{1}}$  is the number of **1** NCs; Fig. 3a). For  $18 < \chi < 25$ , the solid product is only observed within a period of approximately one week (metastable suspension), while the precipitation of aggregates becomes very rapid (visible aggregates < 10 s) when  $\chi > 50$ . These experiments indicate that CB[7] readily chemisorbs to InP/ZnS NCs of **1** surfaces acting as a ‘glue’ to efficiently bring together NCs, forming an interconnected matrix.

To probe the assembly processes, the **1**:CB[7] system is continuously monitored using in situ dynamic light scattering (DLS; Figs. 3b and Supplementary Fig. 11) and electrokinetic zeta ( $\zeta$ ) potential measurements (Fig. 3c) along with TEM for different  $\chi$  values (Figs. 3e and Supplementary Fig. 12). The size of the resultant aggregates can be tuned from the bulk precipitates towards stable colloidal systems as the concentration of CB[7] reduces ( $0 < \chi < 20$ ; Figs. 3a–c). Controlling  $D_h$  of **1**:CB[7] assemblies over a wide range (6–50 nm) can be readily achieved by varying  $\chi$ . Kinetic growth observed by DLS reveals two distinct stages of assembly, with fast initial growth after adding CB[7]. For example, with  $\chi = 9$ , the  $D_h$  value of **1**:CB[7] quickly increases from  $3.3 \pm 0.7$  to  $9.3 \pm 2.8$  nm within the first five

minutes. After this initial stage, the growth slows by a factor of  $\sim 100$ , leading to water-soluble assemblies with  $D_h = 11.8 \pm 3.0$  nm after 20 h (Fig. 3b). The second stage of cluster growth fits the model of Ostwald ripening (Supplementary Fig. 14)<sup>25</sup>. As  $\chi$  approaches 20, assembly accelerates and systems with a higher CB[7] concentration reach the maximum  $D_h$  quicker; for  $\chi > 30$ , the colloids become unstable within 20 h.

Electrokinetic  $\zeta$  potential experiments reveal the self-limiting nature of this CB[*n*]-mediated aggregation. The initial highly negative  $\zeta$  potential of **1** ( $\zeta = -45$  mV) remains unchanged after the addition of CB[7] if  $\chi < 20$  (Fig. 3c), indicating the colloidal stability of emerging **1**:CB[7] assemblies as well as the self-limiting character of their growth<sup>5</sup>. For  $\chi > 20$ , a gradual increase in the  $\zeta$  potential is observed, reaching a moderate level ( $-30 < \zeta < -20$  mV) for  $30 < \chi < 40$  (incipient stability). Even less negative  $\zeta$  potential values ( $\zeta > -10$  mV) are observed when  $\chi > 50$  (unstable colloids).

The stability of  $\zeta$  potential and the ultimate cessation of aggregate growth for  $\chi < 20$  can be rationalized by strong electrostatic repulsion between both emerging aggregates as well as aggregates and NCs of **1** (Fig. 3d). In such systems ( $\chi < 20$ ), smaller aggregates and/or free NCs take part in the stabilization of larger assemblies, adhering to their ‘sticky’ interfaces saturated with CB[7] (Fig. 3d, inset), screening attractive interactions between the latter and acting as dynamic particulate surfactants<sup>6,26–29</sup>. Saturation of the assembled interfaces with CB[7] macrocycles ( $\chi > 20$ ) increases the probability of effective collisions, in which smaller aggregates become glued to larger ones, decreasing the repulsive interactions and subsequently

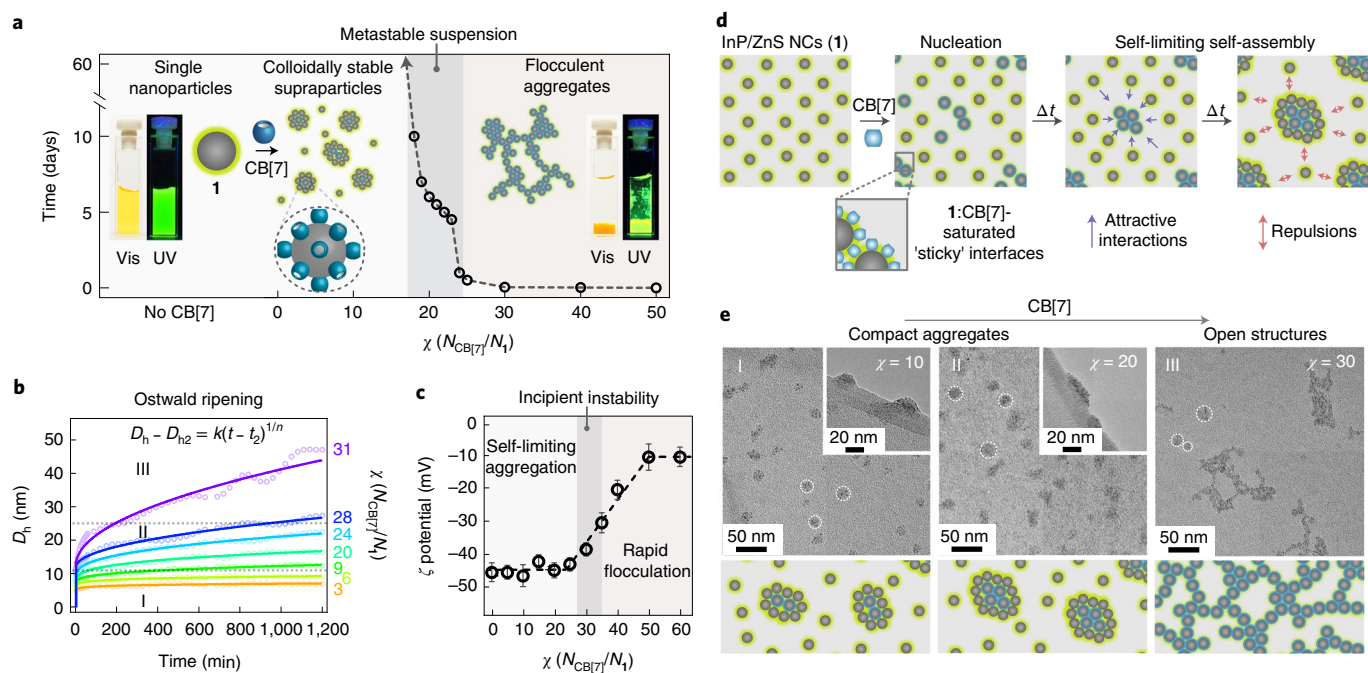


**Fig. 3 | Self-limiting self-assembly of InP/ZnS NCs and CB[7].** **a**, Formation and stability of 1:CB[7] assemblies versus ratio between the number of CB[7] and 1 NCs. Time refers to a point until the formation of observable precipitates was noted. The inset shows an InP/ZnS NC decorated with CB[7] macrocycles as a fragment of the larger 1:CB[7] aggregate. **b**, Evolution of hydrodynamic diameter  $D_h$  in 1:CB[7] monitored by DLS. In the equation,  $D_h$  is hydrodynamic diameter observed at time  $t$ ;  $D_{h2}$  is a starting hydrodynamic diameter at time  $t_2$  (the beginning of the second stage of cluster growth);  $k$  is the constant for a specific material. **c**, Dependence of electrokinetic  $\zeta$  potential on the CB[7]-to-1 NC ratio, namely,  $\chi (N_{CB[7]}/N_1)$ , revealing the self-limiting character of aggregation for  $\chi < 20$ . Data are presented as mean values  $\pm$  s.d. ( $n = 3$ ). **d**, Schematic of the self-limiting processes leading to colloidally stable 1:CB[7] assemblies. The inset shows interfaces of emerging 1:CB[7] aggregates saturated with CB[7] molecular glue. **e**, TEM micrographs of 1:CB[7] aggregates for aliquots taken after 20 h of incubation. The insets show 1:CB[7] aggregates at higher magnification. The bottom panels present schematics of 1:CB[7] aggregates observed by TEM.

leading to flocculation and precipitation. These observations suggest that the colloidally stable 1:CB[7] assemblies for  $\chi < 20$  are likely a result of complex processes and a balance between many different factors, that is, coordination and hydrogen-bond-mediated attractive forces, van der Waals interactions, electrostatic repulsions as well as steric and entropic colloidal stabilization<sup>30</sup>. On the contrary, for  $\chi > 20$ , the assembly processes change, becoming dominated by attractive forces when  $\chi > 40$ .

TEM images of stable suspensions of 1:CB[7] provide structural insights into their morphology (Figs. 3e and Supplementary Fig. 12). Lower CB[7] concentrations (that is,  $\chi = 10$  and  $\chi = 20$ ) lead to quasi-spherical loosely packed clusters with mean diameters in good agreement with the DLS data. As the ratio of CB[7] increases ( $\chi > 20$ ), elongated chain-like fractal structures can be observed, which are the dominant product when  $\chi > 30$  (Fig. 3e). This is likely explained by the assembly shifting from reaction-limited to diffusion-limited aggregation, which ultimately influences the final topology<sup>19</sup>.

**Kinetic arrest of plasmonic assemblies through ISLA.** The propensity of CB[7] to rapidly glue together 1 NCs was further exploited to kinetically arrest the transient states of AuNC aggregates through ISLA processes, yielding hybrid semiconductor–metal nanoassemblies (Fig. 4a).

In an initial experiment, CB[7] was added to a 1:1 v/v mixture of InP/ZnS NCs (10  $\mu$ M;  $\chi = 100$ ) and AuNCs **2a** (12 nm; 0.010  $\mu$ M). This yielded red aggregates within seconds, which quantitatively precipitated after  $\sim 30$  min (**2a:CB[7]:1-Red**; Supplementary Fig. 14). Alternatively, when CB[7] was first mixed with **2a**, followed by the addition of **1** (all in the same ratios), a dark-blue precipitate was

observed (**2a:CB[7]:1-Blue**; Supplementary Fig. 16). TEM images of these two materials (Supplementary Figs. 15 and 17) highlight the structural differences between them. Evidently, **2a:CB[7]:1-Red** contains single AuNCs, which are well dispersed throughout a loosely packed 1:CB[7] matrix, while **2a:CB[7]:1-Blue** consists of chain-like assemblies of AuNCs trapped within the 1:CB[7] array. This set of experiments confirms that InP/ZnS NCs can be used as an efficient modulator of CB[ $n$ ]-mediated aggregation of AuNCs (ref. 19).

For direct monitoring of the ISLA-assisted assembly, we employ larger AuNCs (**2b**; 60 nm) that offer good separation between the UV–visible (UV–vis) absorption bands characteristic of monomers (localized surface plasmon resonance band at 535 nm; Fig. 4b), dimers (660 nm) and large aggregates (680–900 nm) (ref. 19). The formation of colloidally stable AuNC:CB[7]:InP/ZnSNC hybrids is comprehensively studied by UV–vis spectroscopy, DLS, electrokinetic  $\zeta$  potential and electron microscopy experiments. The self-assembly of **2b:CB[7]:1** hybrids is triggered by the addition of CB[7] to a suspension of AuNCs (**2b**). The rate of aggregation is reflected in the progressive decrease in the localized surface plasmon resonance band intensity of single AuNCs and the subsequent appearance of dimer and long-chain modes (Fig. 4b). The injection of **1** NCs into the suspension during AuNC self-assembly leads to the efficient arrest of growth, trapping the **2b:CB[7]** aggregates within the 1:CB[7] arrays, visible by the stabilization of absorbance at 535 nm. Once **2b:CB[7]** assemblies are arrested, the resulting **2b:CB[7]:1** hybrids demonstrate extended stability of their optical properties for weeks, with no further changes observed in the UV–vis spectra (Fig. 4b, Supplementary Fig. 18, and Fig. 4e, inset). In contrast, in the absence of InP/ZnS NCs, **2b:CB[7]** aggregates continue to grow resulting in precipitation after 30–60 min.

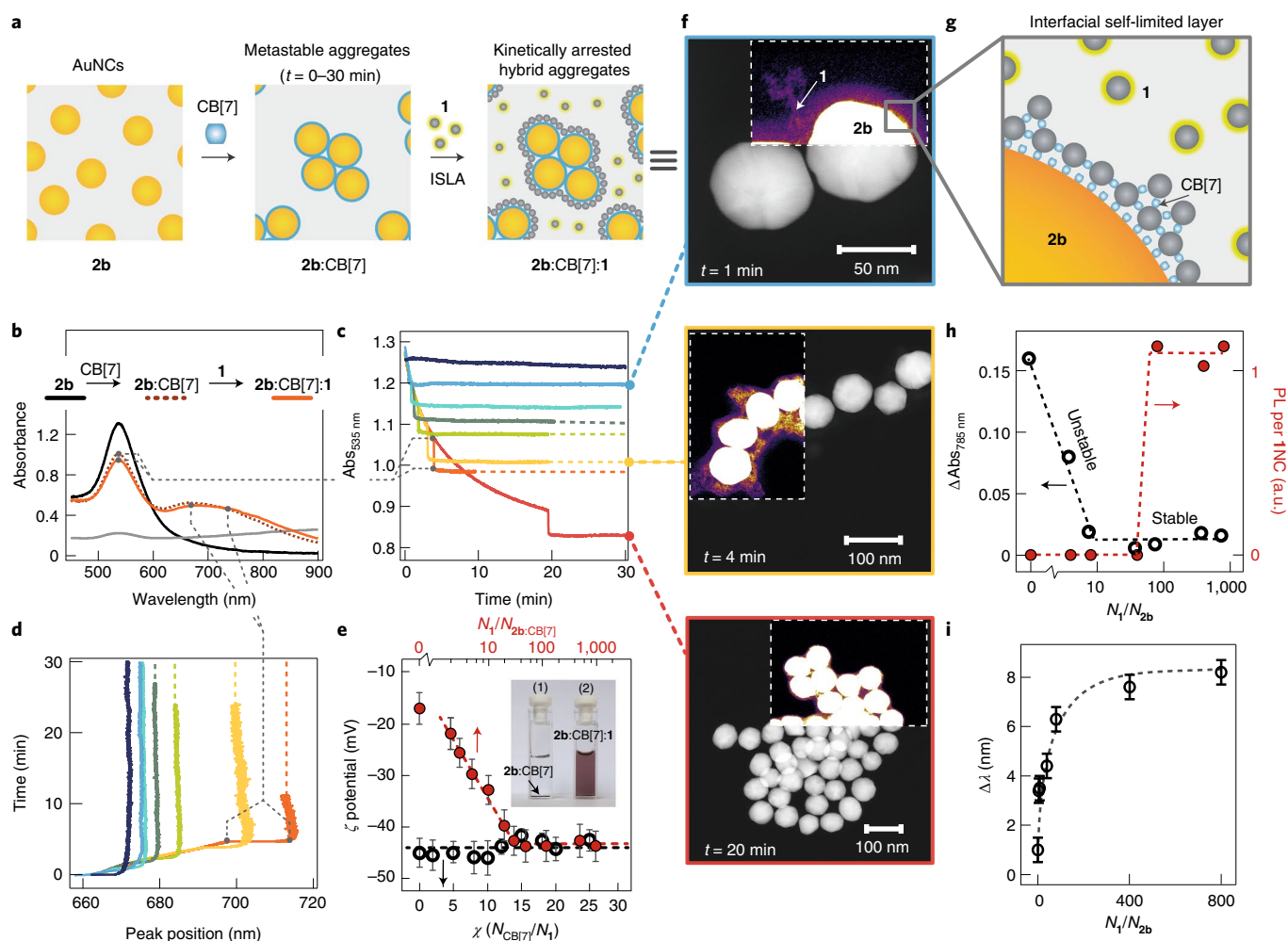


**Fig. 4 | Overview of kinetic arrest of plasmonic assemblies through ISLA and the formation of hybrid systems.** **a**, Schematic of ISLA-mediated kinetic arrest of emerging AuNC aggregates and stabilization of semiconductor–plasmonic hybrids. **b**, Typical UV-vis spectra of single AuNCs (**2b**, black), **2b**:CB[7] aggregates after 10 min of CB[7]-mediated assembly (dashed orange), the same system immediately after injecting **1** to form **2b**:CB[7]:**1** hybrid (orange; note that this UV-vis characteristic is retained for several weeks) and system of **2b** and CB[7] (no **1** NCs) after 30 min of incubation (grey). **c**, **d** Time evolution of absorbance at 535 nm ( $Abs_{535\text{nm}}$ ) (**c**) and spectral position of coupled mode resonance peak during **2b**:CB[7] aggregation with the addition of **1** at various time points (**d**). **e**, Changes in the electrokinetic  $\zeta$  potential of **2b**:CB[7] aggregates on the addition of **1** (red); for  $N_1/N_{2b:CB[7]} > 20$ , the  $\zeta$  potential values are characteristic of **1**:CB[7] aggregates from a self-limiting aggregation regime (black). Data are presented as mean values  $\pm$  s.d. ( $n=3$ ). **f**, Representative STEM images of **2b**:CB[7] aggregates entrapped within **1**:CB[7] arrays at different stages of aggregation; insets show **1**:CB[7] arrays by contrast colour scaling. **g**, Schematic representing the interfaces of **2b**:CB[7]:**1** aggregates, emphasizing the role of the interfacial self-limited layer of **1**:CB[7] arrays. **h**, Evolution of coupled mode absorbance at 785 nm, 15 min after the addition of **1** to **2b**:CB[7] (black) and normalized PL at 526 nm from 377 nm excitation (red) against the number ratio between **1** and **2b** ( $N_1/N_{2b}$ ). **i**, Spectral peak shift in the coupled mode resonance versus  $N_1/N_{2b}$ . The error bars are generated from the fitting of the mode positions.

The colloidal stability of **2b**:CB[7] aggregates is shown by changes in  $\zeta$  potential on the addition of **1** NCs (Fig. 4e). Colloids of **2b** AuNCs are inherently stable with a  $\zeta$  potential of  $-45$  mV. The addition of relatively small quantities of CB[7] (that is,  $10^3$  molecules per NC (**2b**); surface coverage,  $\sim 10\%$ ) destabilizes the system, leading to the aggregation of plasmonic NCs and an increase in  $\zeta$  potential to  $-17$  mV. The colloidal stability of the resultant system is restored by the addition of **1** NCs ( $>20$  per **2b** NC), followed by changes in the  $\zeta$  potential to values characteristic of the starting materials, that is, around  $-45$  mV.

The size of these stable hybrids can be controlled by adding **1** at a specific time, once the desired level of **2b**:CB[7] aggregation is reached (Fig. 4c,d). The typical morphology of the resulting **2b**:CB[7]:**1** hybrids is visualized using electron microscopy (Fig. 4f and Supplementary Fig. 19), revealing individual AuNC aggregates decorated with **1** NCs. For example, dimeric species are observed as

the main fraction of the system when aggregation is stopped after 60 s (Fig. 4f, top). Larger assemblies, typically incorporating 4–8 or 20–40 NCs of **2b**, are found for systems in which growth was terminated after 4 and 20 min, respectively. This is on account of the rapid formation of a CB[7]:**1** layer through self-limiting processes at the interfaces of **2b**:CB[7] aggregates (Fig. 4g,f), preventing attractive interactions between **2b**:CB[7] cores. In these systems, the InP/ZnS NCs can be regarded as stabilizing surfactants<sup>6,26–29</sup>, which absorb excess CB[7] molecules and passivate the interfaces of AuNC:CB[7] assemblies, halting further aggregation.

Evolution of the refractive index (RI) and the optical properties of AuNC aggregates on the addition of **1** provides further insights into the interfacial composition of **2b**:CB[7]:**1** hybrids (Fig. 4c,d,h,i and Supplementary Figs. 20 and 21). The redshift in the coupled mode resonance ( $\sim 785$  nm) of **2b**:CB[7] assemblies (Fig. 4c,i) reflects an increase in their surrounding RI and is a direct indication of the

decoration of AuNC surfaces with high-RI semiconductor NCs ( $RI_{\text{InP}}=2.4$ ) (refs. <sup>31,32</sup>). Moreover, monitoring the evolution of the coupled mode absorbance at 785 nm for systems with different **1:2b** ratios ( $N_1/N_{2b}$ ) shows that the stabilization of the optical properties of **2b:CB[7]** aggregates is achieved for  $N_1/N_{2b} > 10$  (Fig. 4h); this is in line with the electrokinetic  $\zeta$  potential measurements, which indicate the recovery of colloidal stability for  $N_1/N_{2b} > 20$  (Fig. 4e).

**Tracking light-driven out-of-equilibrium redox chemistry at nanoparticle interfaces.** Spatial confinement of the photocatalytically active InP/ZnS NCs **1** with plasmonic AuNC antennae **2b** (Fig. 5a) was explored as a multifunctional colloidal substrate for the real-time observation of photogenerated radical species via operando SERS.

Methyl viologen ( $MV^{2+}$ ) was selected as a model electron acceptor on account of its well-studied redox chemistry (Fig. 5b) and Raman activity<sup>33,34</sup>. The one-electron reduction of  $MV^{2+}$  to a radical cation ( $MV^+$ ) makes it an efficient electron mediator (EM), attracting enormous attention for photocatalysis, electrochromic devices, solar energy conversion systems, batteries and molecular machines<sup>33–38</sup>. However, despite their widespread application and extensive reports on their redox properties, the assembly of  $MV^+$  radicals and structures of the resultant dimeric species remain poorly understood. Geraskina et al. recently reported that  $MV$  sigma dimers (4,4', 2,2' and 2,4; Fig. 5b) could not be formed under thermodynamic conditions on account of extremely high calculated free energies of binding<sup>39</sup>. Herein we report—to the best of our knowledge—the first direct observation of the formation of  $MV$  sigma dimers under out-of-equilibrium conditions at room temperature using **2b:CB[7]:1** assemblies.

The hybrid aggregates incorporating  $MV^{2+}$  were prepared by the simple addition of EM ( $MV^{2+}$ ) to a deoxygenated aqueous suspension of **2b:CB[7]:1** (molar concentration  $c_{MV^{2+}}=1.6\mu\text{M}$ ;  $MV^{2+}:CB[n]$  molar ratio, 1:1).  $MV^{2+}$  adsorbs to the **2b:CB[7]:1** interfaces (Supplementary Fig. 43) with an estimated surface density of one  $MV^{2+}$  molecule per five square nanometres to form a **2b:CB[7]:1**  $\subset$   $MV^{2+}$  supramolecular system. The resultant stable suspension was uniformly illuminated with excitation at  $\lambda=302\text{ nm}$  (pump light, generating excited electrons within **1** NCs), while operando SERS was probed using a 785 nm laser (probe light; Supplementary Fig. 42).

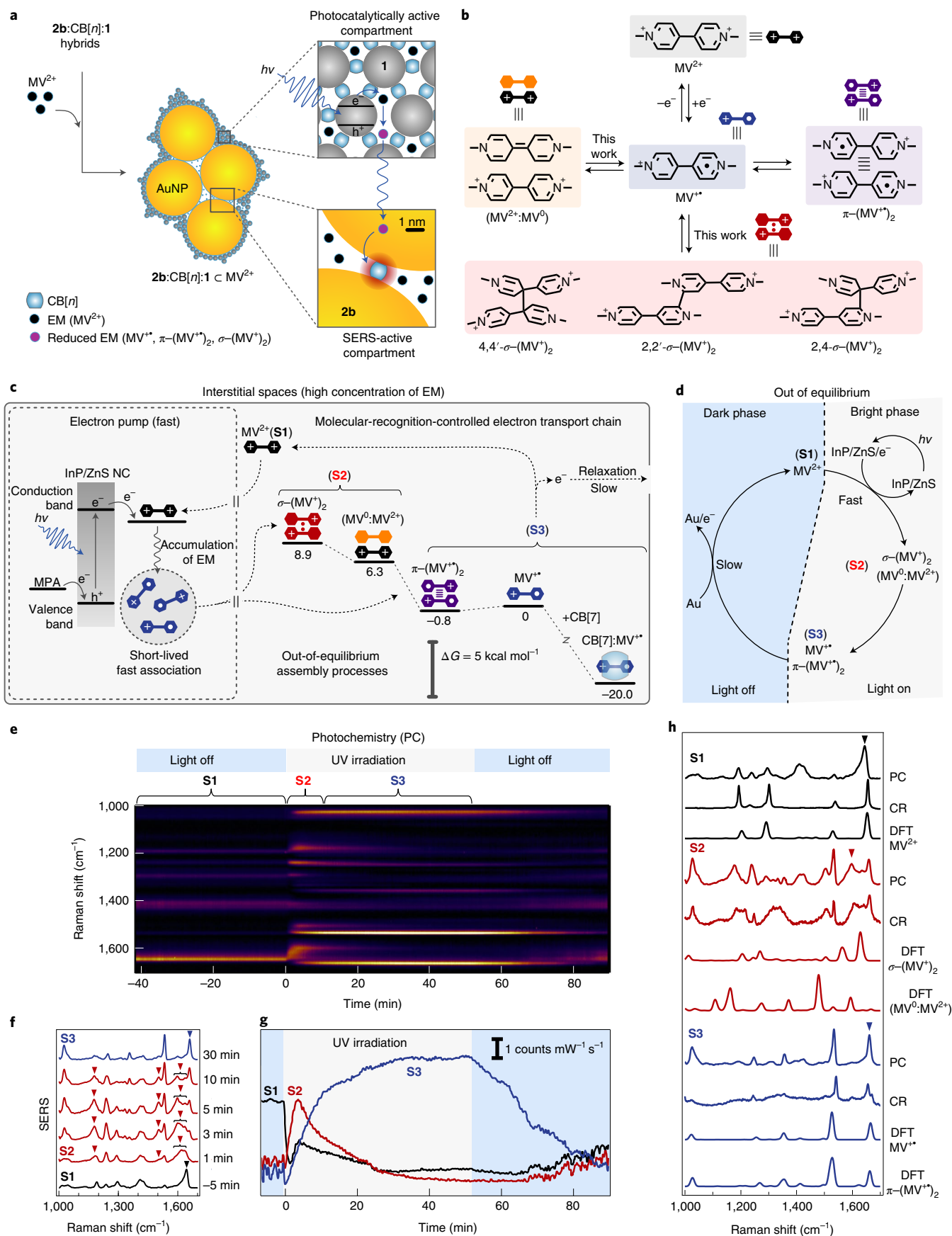
An overview of photoinduced interfacial transformations is shown in Fig. 5c,d. Photoirradiation of the **2b:CB[7]:1**  $\subset$   $MV^{2+}$  system generates high-energy electrons within **1** NCs, which are immediately transferred to chemisorbed  $MV^{2+}$  (state 1; **S1**), undergoing reduction to form  $MV^+$  monoradical cations. The initial high local concentration and spatial confinement of the photogenerated products promote their fast (below the temporal resolution of the instrument) association, leading to the formation of elusive  $\sigma$ -( $MV^+$ )<sub>2</sub> dimeric species and [ $MV^{2+}:MV^0$ ] heterobinary complexes (state 2; **S2**) as well as classical  $\pi$ -( $MV^+$ )<sub>2</sub> dimers and monoradical  $MV^+$  cations (state 3; **S3**) (ref. <sup>39</sup>). Both dimeric species undergo

further dissociation to form  $MV^+$ , which, in the case of **2b:CB[7]:1**, is promoted by their encapsulation within the CB[7] cavity to form thermodynamically stable 1:1 complexes<sup>40</sup>. Before ultimately returning to their ground state, the photogenerated radicals can relax by donating an electron to the Fermi level in **2b** AuNCs (ref. <sup>41</sup>). Notably, the photogeneration of  $MV^+$  should be characterized by different reaction rates in comparison to AuNC-mediated relaxation; therefore, two distinct phases of non-equilibrium processes are anticipated (Fig. 5d): (1) a light-driven bright phase leading to the accumulation of photogenerated products; (2) a dark phase controlled by relaxation processes.

The kinetics of these photochemical processes are directly revealed through real-time SERS spectra (Fig. 5e–h). The attribution of the observed sets of vibrational peaks is supported by density functional theory (DFT) calculations and, where possible, by Raman spectroscopy experiments for bulk aqueous  $MV^{2+}$  solutions in the absence and presence of a chemical reducing agent (Fig. 5h and Supplementary Figs. 45 and 46). In the absence of UV irradiation (from  $t=-40$  to  $t=0$  min; Fig. 5e), the SERS intensity of  $MV^{2+}$  (**S1**; assigned to the diagnostic peak at  $1,643\text{ cm}^{-1}$ ) is found to be stable under exposure to the 785 nm probe laser. Introduction of the pump light ( $\lambda=302\text{ nm}$ ) leads to the evolution of three specific states (**S1–S3**) with distinct spectral features (Fig. 5e–g; also see Supplementary Fig. 47 and the discussion therein). An immediate decrease in the SERS intensity of  $MV^{2+}$  is first observed, accompanied with corresponding intensity increases from SERS bands attributed to a mixture of  $MV^+$  and  $\pi$ -( $MV^+$ )<sub>2</sub> (**S3**), denoted by the diagnostic Raman resonance at  $1,660\text{ cm}^{-1}$ . Interestingly, additional bands are observed between  $1,600$  and  $1,640\text{ cm}^{-1}$  as well as at  $1,504$  and  $1,180\text{ cm}^{-1}$  (Fig. 5f), which have a different kinetic profile from states **S1** and **S3**. These bands were attributed to the elusive dimeric species connected by a sigma bond,  $\sigma$ -( $MV^+$ )<sub>2</sub>, as well as the [ $MV^{2+}:MV^0$ ] pair (ref. <sup>42</sup>), as corroborated by DFT calculations (Fig. 5h and Supplementary Figs. 29 and 46). Signals characteristic for state **S2** saturate after 4 min, which is followed by a decrease in their intensity, indicating the dominance of dissociation of the  $\sigma$ -( $MV^+$ )<sub>2</sub> dimer and comproportionation<sup>43</sup> of the [ $MV^{2+}:MV^0$ ] species. Both these processes further contribute to the population of  $MV^+$  radical cations, increasing their concentration before reaching saturation ( $t=35\text{ min}$ ).

In the described **2b:CB[7]:1** system, decreasing concentrations of  $\sigma$ -( $MV^+$ )<sub>2</sub> and [ $MV^{2+}:MV^0$ ] result from the efficient encapsulation of  $MV^+$  radical cations within CB[7] (ref. <sup>40</sup>), which shifts the local equilibrium towards the monomeric  $MV$  states as corroborated by free energy of binding calculations ( $\Delta G$ ; Fig. 5c and Supplementary Figs. 24–39). On the removal of pump light, the system is switched from an out-of-equilibrium light-driven phase (bright phase; Fig. 5c) to an equilibrated state (dark phase). This is associated with a decrease in the intensity of  $MV^+$  signal and a corresponding increase in the intensity of  $MV^{2+}$  signal, a result of the relaxation of the system<sup>41</sup>.

**Fig. 5 | Tracking light-driven out-of-equilibrium redox chemistry within hybrid aggregates.** **a**, Schematic of hybrid aggregates emphasizing the role of their compartmentalization and sorption capabilities. **b**, Redox chemistry of methyl viologen as a molecular electron mediator (EM). **c**, Out-of-equilibrium electron transfer within the hybrids with free energies of binding for all the observed products, depicting the significance of molecular recognition for controlling these processes. Light-induced electron reduction of  $MV^{2+}$  mediated by InP/ZnS NCs of **1** (state **S1**) leads to the formation of  $MV^+$  radicals, which undergo further fast association processes to form elusive  $\sigma$ -( $MV^+$ )<sub>2</sub> and [ $MV^{2+}:MV^0$ ] species (state **S2**) and classical  $\pi$ -( $MV^+$ )<sub>2</sub> dimers (state **S3**). Dissociation of dimeric species is promoted by the encapsulation of  $MV^+$  within CB[7] macrocycles.  $MV^+$  can further slowly relax by oxidation reactions to regenerate  $MV^{2+}$  species. **d**, A photochemical cycle within the hybrids and its division into bright and dark phases. **e**, Real-time SERS monitoring of  $MV^{2+}$  photochemistry within the hybrid aggregates, with UV irradiation time period marked by a blue bar. **f**, Selected spectra from the photochemistry SERS time scan showing the distinct spectra for three different states. Triangles mark the diagnostic peak positions representative for each species used for fitting; respective time stamps are displayed on the right axis. **g**, Photochemical kinetics of each species (**S1**, black,  $MV^{2+}$ ,  $1,643\text{ cm}^{-1}$ ; **S2**, red,  $\sigma$ -( $MV^+$ )<sub>2</sub>/[ $MV^{2+}:MV^0$ ],  $1,600\text{ cm}^{-1}$ ; **S3**, blue,  $MV^+/\pi$ -( $MV^+$ )<sub>2</sub>,  $1,660\text{ cm}^{-1}$ ) extracted through multi-Gaussian fitting. **h**, Comparison of spectra obtained from photochemistry (PC), chemical reduction (CR) and DFT calculations for different  $MV$  species.



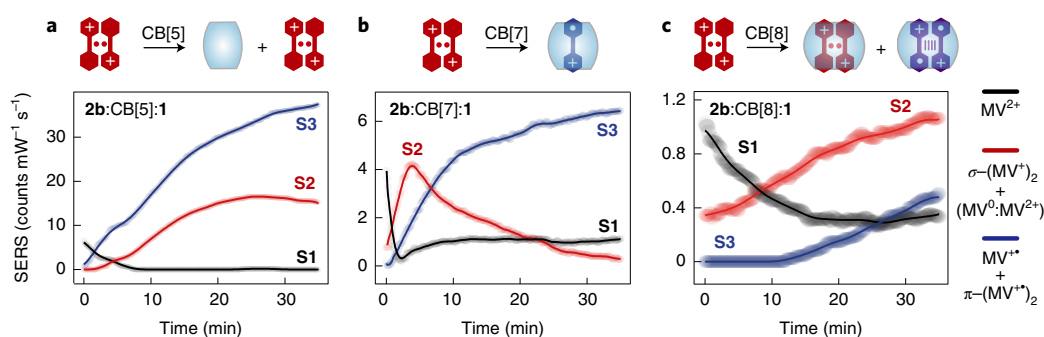


**Fig. 6 | Real-time monitoring of light-induced redox-driven molecular recognition processes.** **a–c**, Photochemical kinetics of each species extracted through multi-Gaussian fitting for **2b:CB[5]:1** (**a**), **2b:CB[7]:1** (**b**) and **2b:CB[8]:1** (**c**).

### Supramolecular control of light-induced redox-driven processes at colloidal interfaces.

Variation in the cavity size of CB[*n*] (*n* = 5–8) can be used to control the binding and complexation of analytes as a function of the homologue. The cavity of CB[5], for example, is too small to accommodate any viologen derivative<sup>20</sup>. Therefore, when CB[5] is employed as the gluing agent (**2b:CB[5]:1**  $\subset$  MV<sup>2+</sup>), all the light-induced chemical processes occur outside the cavity. We anticipated that in such a system, the lifetime of photogenerated  $\sigma$ -(MV<sup>+</sup>)<sub>2</sub> dimers and [MV<sup>2+</sup>:MV<sup>0</sup>] species will be higher compared with the hybrids based on the larger CB[7] macrocycle. Indeed, for the CB[5]-based system, a signal decrease for MV<sup>2+</sup> is observed on UV irradiation, which is accompanied with a rise in the SERS intensity from  $\sigma$ -(MV<sup>+</sup>)<sub>2</sub>/[MV<sup>2+</sup>:MV<sup>0</sup>] (**S2**) and MV<sup>+</sup>/ $\pi$ -(MV<sup>+</sup>)<sub>2</sub> (**S3**) (Fig. 6a and Supplementary Fig. 44). Notably, signals from state **S2** are found to be relatively stable, saturating after ~25 min, highlighting that when out-of-equilibrium reaction conditions are applied (bright phase), the thermodynamically unstable  $\sigma$ -(MV<sup>+</sup>)<sub>2</sub> and [MV<sup>2+</sup>:MV<sup>0</sup>] species can accumulate within the hybrid aggregates.

In contrast, the CB[7] spacer has a large enough cavity to encapsulate a single MV<sup>2+</sup>, MV<sup>+</sup> or MV<sup>0</sup> species, forming binary 1:1 host–guest complexes<sup>40</sup>. Within CB[7]-bridged **2b:CB[7]:1**  $\subset$  MV<sup>2+</sup> hybrid aggregates, the formation of dimeric species is suppressed, which is reflected by the early saturation point of **S2** (Fig. 6b; *t* = 4 min). In this system, CB[7] macrocycles promote the dissociation of  $\sigma$ -(MV<sup>+</sup>)<sub>2</sub> dimers and [MV<sup>2+</sup>:MV<sup>0</sup>] pair by sequestering MV<sup>+</sup> radical cations within their molecular cavities.

The larger CB[8] homologue not only accommodates MV<sup>2+</sup> within a 1:1 host–guest complex but also enhances the dimerization of MV<sup>+</sup> through encapsulation. Indeed, within a hybrid aggregate held together with CB[8] (**2b:CB[8]:1**  $\subset$  MV<sup>2+</sup>), the continuous generation of dimeric species is observed from the onset of photoexcitation (Fig. 6c and Supplementary Fig. 44). Notably, the appearance of signals characteristic of MV<sup>+</sup>/ $\pi$ -(MV<sup>+</sup>)<sub>2</sub> (**S3**) is significantly delayed and occurs after only 12 min. This is likely a result of retaining stabilized  $\sigma$ -(MV<sup>+</sup>)<sub>2</sub> dimers (Fig. 5j) within CB[8] in the first stage of the bright phase and thus the subsequent suppression of MV<sup>+</sup> population (Fig. 6c).

**Conclusions.** We demonstrate a new assembly strategy leading to the formation of photoactive, colloidal stable hybrid materials consisting of semiconductor and plasmonic NCs. Rapid hybridization is accomplished through the ISLA of semiconductor NCs, which adsorb on the surfaces of growing AuNC aggregates through subnanometre CB[*n*] (*n* = 5–8) molecular bridges. As CB[*n*] is able to mediate the assembly of both semiconductor and plasmonic NCs, a wide array of new hybrid systems can be readily prepared with implicit control over the morphology and optical properties. These systems efficiently harvest light within the semiconductor substructures, inducing out-of-equilibrium electron transfer

processes, the products of which can be simultaneously detected through the incorporated SERS-active AuNC antennae. This functional compartmentalization alongside the spatial confinement of an EM, namely, MV<sup>2+</sup>, within the interstitial spaces of the hybrids enables the direct observation of various out-of-equilibrium photochemical transformations in real time. The light-controlled generation of MV radical species and their subsequent assembly directed by molecular-recognition-driven intermolecular electron transfer reveals the formation of long-overlooked, elusive  $\sigma$ -(MV<sup>+</sup>)<sub>2</sub> dimeric species. The impressive colloidal stability, dynamic character and permeability of CB[*n*]-bridged hybrid constructs enabled—for the first time—the in situ tracking of complex chemistries of open-shell radicals strictly controlled by host–guest interactions. As our strategy reveals exclusively chemical species confined within the aggregates and located in close proximity to AuNC surfaces (<2 nm), the reported hybrid systems can also be regarded as a prototypical colloidal nano(photo)electrode, serving as a powerful platform for the direct and precise visualization of redox chemistry at metal/water and semiconductor/water interfaces. These findings pave the way for widespread use of such hybrids for the long-term, real-time tracking of interfacial charge transfer processes, that is, the light-driven generation of radicals and catalysis with operando spectroscopies under out-of-equilibrium conditions.

### Online content

Any methods, additional references, Nature Research reporting summaries, source data, extended data, supplementary information, acknowledgements, peer review information; details of author contributions and competing interests; and statements of data and code availability are available at <https://doi.org/10.1038/s41565-021-00949-6>.

Received: 17 December 2019; Accepted: 30 June 2021;

Published online: 2 September 2021

### References

- Jiang, R., Li, B., Fang, C. & Wang, J. Metal/semiconductor hybrid nanostructures for plasmon-enhanced applications. *Adv. Mater.* **26**, 5274–5309 (2014).
- Lim, E.-K. et al. Nanomaterials for theranostics: recent advances and future challenges. *Chem. Rev.* **115**, 327–394 (2015).
- Boles, M., Engel, M. & Talapin, D. Self-assembly of colloidal nanocrystals: from intricate structures to functional materials. *Chem. Rev.* **116**, 11220–11289 (2016).
- Boles, M., Ling, D., Hyeon, T. & Talapin, D. The surface science of nanocrystals. *Nat. Mater.* **15**, 141–153 (2016).
- Xia, Y. et al. Self-assembly of self-limiting monodisperse supraparticles from polydisperse nanoparticles. *Nat. Nanotechnol.* **6**, 580–587 (2011).
- Kalsin, A. et al. Electrostatic self-assembly of binary nanoparticle crystals with a diamond-like lattice. *Science* **312**, 420–424 (2006).

7. André, A. et al. Toward conductive mesocrystalline assemblies: PbS nanocrystals cross-linked with tetrathiafulvalene dicarboxylate. *Chem. Mater.* **27**, 8105–8115 (2015).
8. Connolly, S. & Fitzmaurice, D. Programmed assembly of gold nanocrystals in aqueous solution. *Adv. Mater.* **11**, 1202–1205 (1999).
9. Macfarlane, R., O'Brien, M., Petrosko, S. & Mirkin, C. Nucleic acid-modified nanostructures as programmable atom equivalents: forging a new 'table of elements'. *Angew. Chem. Int. Ed.* **52**, 5688–5698 (2013).
10. Wang, Y. et al. Host–guest chemistry with water-soluble gold nanoparticle supraspheres. *Nat. Nanotechnol.* **12**, 170–176 (2017).
11. Sánchez-Iglesias, A. et al. Hydrophobic interactions modulate self-assembly of nanoparticles. *ACS Nano* **6**, 11059–11065 (2012).
12. Choueiri, R. M., Klinkova, A., Thérien-Aubin, H., Rubinstein, M. & Kumacheva, E. Structural transitions in nanoparticle assemblies governed by competing nanoscale forces. *J. Am. Chem. Soc.* **135**, 10262–10265 (2013).
13. Jia, G. et al. Couples of colloidal semiconductor nanorods formed by self-limited assembly. *Nat. Mater.* **13**, 301–307 (2014).
14. de Q. Silveira, G. et al. Supraparticle nanoassemblies with enzymes. *Chem. Mater.* **31**, 7493–7500 (2019).
15. Banin, U. & Sitt, A. Colloidal self-assembly: superparticles get complex. *Nat. Mater.* **11**, 1009–1011 (2012).
16. Yi, C. et al. Self-limiting directional nanoparticle bonding governed by reaction stoichiometry. *Science* **369**, 1369–1374 (2020).
17. Yao, G. et al. Programming nanoparticle valence bonds with single-stranded DNA encoders. *Nat. Mater.* **19**, 781–788 (2020).
18. Jehannin, M., Rao, A. & Cölfen, H. New horizons of nonclassical crystallization. *J. Am. Chem. Soc.* **141**, 10120–10136 (2019).
19. Taylor, R. et al. Precise subnanometer plasmonic junctions for SERS within gold nanoparticle assemblies using cucurbit[*n*]uril 'glue'. *ACS Nano* **5**, 3878–3887 (2011).
20. Barrow, S., Kasper, S., Rowland, M., Del Barrio, J. & Scherman, O. A. Cucurbituril-based molecular recognition. *Chem. Rev.* **115**, 12320–12406 (2015).
21. Chikkaraddy, R. et al. Single-molecule strong coupling at room temperature in plasmonic nanocavities. *Nature* **535**, 127–130 (2016).
22. Jing, L. et al. Aqueous based semiconductor nanocrystals. *Chem. Rev.* **116**, 10623–10730 (2016).
23. Ni, X.-L. et al. Cucurbit[*n*]uril-based coordination chemistry: from simple coordination complexes to novel poly-dimensional coordination polymers. *Chem. Soc. Rev.* **42**, 9480–9508 (2013).
24. Ziegler, C. et al. Modern inorganic aerogels. *Angew. Chem. Int. Ed.* **56**, 13200–13221 (2017).
25. Huang, F., Zhang, H. & Banfield, J. F. Two-stage crystal-growth kinetics observed during hydrothermal coarsening of nanocrystalline ZnS. *Nano Lett.* **3**, 373–378 (2003).
26. Yang, Z., Wei, J., Sobolev, Y. I. & Grzybowski, B. A. Systems of mechanized and reactive droplets powered by multi-responsive surfactants. *Nature* **553**, 313–318 (2018).
27. Kowalczyk, B. et al. Charged nanoparticles as supramolecular surfactants for controlling the growth and stability of microcrystals. *Nat. Mater.* **11**, 227–232 (2012).
28. Liu, X. et al. Reconfigurable ferromagnetic liquid droplets. *Science* **365**, 264–267 (2019).
29. Cui, M., Emrick, T. & Russell, T. P. Stabilizing liquid drops in nonequilibrium shapes by the interfacial jamming of nanoparticles. *Science* **342**, 460–463 (2013).
30. Silvera Batista, C. A., Larson, R. G. & Kotov, N. A. Nonadditivity of nanoparticle interactions. *Science* **350**, 176–187 (2015).
31. Homola, J. Surface plasmon resonance sensors for detection of chemical and biological species. *Chem. Rev.* **108**, 462–493 (2008).
32. Wang, Y. et al. Self-assembly and structure of directly imaged inorganic-anion monolayers on a gold nanoparticle. *J. Am. Chem. Soc.* **131**, 17412–17422 (2009).
33. Monk, P. M. S. *The Viologens: Physicochemical Properties, Synthesis and Applications of the Salts of 4,4'-Bipyridine* (Wiley-VCH, 1999).
34. Striepe, L. & Baumgartner, T. Viologens and their application as functional materials. *Chem. Eur. J.* **23**, 16924–16940 (2017).
35. McCune, J. A., Kuehnel, M. F., Reisner, E. & Scherman, O. A. Stimuli-mediated ultrastable radical formation. *Chem* **6**, 1819–1830 (2020).
36. Trabolzi, A. et al. Radically enhanced molecular recognition. *Nat. Chem.* **2**, 42–49 (2010).
37. Bruns, C. J. & Stoddart, J. F. *The Nature of the Mechanical Bond: From Molecules to Machines* (Wiley-VCH, 2016).
38. Cieślak, A. M. et al. Photo-induced interfacial electron transfer of ZnO nanocrystals to control supramolecular assembly in water. *Nanoscale* **9**, 16128–16132 (2017).
39. Geraskina, M., Dutton, A., Juetten, M., Wood, S. & Winter, A. The viologen cation radical pimer: a case of dispersion-driven bonding. *Angew. Chem. Int. Ed.* **56**, 9435–9439 (2017).
40. Kim, H.-J., Jeon, W. S., Ko, Y. H. & Kim, K. Inclusion of methylviologen in cucurbit[7]uril. *Proc. Natl Acad. Sci. USA* **99**, 5007–5011 (2002).
41. Meisel, D., Mulac, W. A. & Matheson, M. S. Catalysis of methyl viologen radical reactions by polymer-stabilized gold sols. *J. Phys. Chem.* **85**, 179–187 (1981).
42. Bockman, T. M. & Kochi, J. K. Isolation and oxidation-reduction of methylviologen cation radicals. Novel disproportionation in charge-transfer salts by X-ray crystallography. *J. Org. Chem.* **55**, 4127–4135 (1990).
43. Norton, J. D. & White, H. S. Effect of comproportionation on the voltammetric reduction of methyl viologen in low ionic strength solutions. *J. Electroanal. Chem.* **325**, 341–350 (1992).

**Publisher's note** Springer Nature remains neutral with regard to jurisdictional claims in published maps and institutional affiliations.

© Crown 2021

## Methods

**Materials.** All chemicals were purchased from Sigma-Aldrich, unless stated otherwise, at the highest purity available and used as received: tris(trimethylsilyl) phosphine (P(TMS)<sub>3</sub>; 95%), 1-octylamine (99%), 1-octadecene (ODE; >95%), indium acetate [In(OAc)<sub>3</sub>; 99.99%], myristic acid (>99%), zinc stearate (purum; 10–12% Zn basis), sulfur (99.998%), 3-mercaptopropionic acid (3-MPA; >99%), sodium carbonate (>99%), gold (III) chloride trihydrate (HAuCl<sub>4</sub> · 3H<sub>2</sub>O; 99.9%), trisodium citrate dihydrate (>99.5%), methyl viologen dichloride (98.0%), ammonia acetate (30%), sodium hydroxide (>97.0%) and sodium hydrosulfite (>82%). ODE was degassed using a Schlenk line under a vacuum at 100 °C (12 h) and purged with N<sub>2</sub> (<5 ppm of oxygen; 1 h). 1-Octylamine was degassed using a Schlenk line under a vacuum at 25 °C (12 h) and purged with N<sub>2</sub> (<5 ppm of oxygen; 1 h). Milli-Q water (18.2 MΩ cm) was used for the preparation of all non-deuterated aqueous solutions. A desired CB[*n*] value was separated from the synthesized CB[*n*] mixture by using literature procedures<sup>44</sup>.

**Preparation of InP/ZnS core-shell NCs.** Water-soluble InP/ZnS core-shell NCs (**1**) were prepared by ligand exchange from their organic-solvent-soluble counterparts and transferred to a water environment. Organic-solvent-soluble InP/ZnS core-shell NCs coated with long-chain carboxylate ligands were prepared according to a modified literature procedure<sup>45</sup>. Details of the synthesis and determination of NC concentrations are available in the Supplementary Information.

**Preparation of citrate-coated AuNCs.** Citrate-coated AuNCs with a diameter of 60 nm (**2b**) were purchased from BBI Solutions and used as received. AuNCs with a diameter of 12 nm (**2a**) were synthesized using a modified Turkevich method<sup>46</sup>. Details of the synthesis and determination of AuNC concentrations are available in the Supplementary Information.

**Characterization of NCs and their assemblies.** TEM was carried out on an FEI Philips Tecnai 20 instrument. Samples were prepared on holey carbon grids by the drop-casting of a desired aqueous solution. STEM was carried out using an FEI Osiris microscope (Thermo Fisher Scientific) equipped with a high-brightness 'X-FEG' electron source and operated at 200 kV. The beam convergence semi-angle was set to 11.0 mrad. DLS was carried out on a Malvern Zetasizer Nano ZS90 instrument fitted with a He-Ne laser ( $\lambda = 663$  nm) at 25 °C. Hydrodynamic diameters ( $D_h$ ) were calculated according to the Stokes-Einstein equation. Fourier transform infrared (FTIR) spectroscopy was performed using a PerkinElmer Spectrum 100 series FTIR spectrometer equipped with a universal ATR sampling accessory. Elemental analysis was performed using a PerkinElmer 240 elemental analyser. <sup>1</sup>H NMR spectra were recorded using a Bruker AVANCE 500 with a TCI Cryoprobe system (500 MHz). Chemical shifts were recorded in parts per million in D<sub>2</sub>O with internal reference set to the solvent peak at  $\delta = 4.79$  ppm. Steady-state UV-vis spectra were recorded on a Varian Cary 4000 UV-vis spectrophotometer in aqueous solutions with 1 nm resolution at 25 °C. Steady-state photoluminescence (PL) spectroscopy was realized by illuminating the cuvette-held sample using a diode laser (Coherent CUBE) with an emission wavelength of 377 nm. The PL signal was collected using a lens into a multimode fibre and recorded by an Ocean Optics QE65000 spectrometer.

**Studies on aggregation of InP/ZnS NCs (**1**) mediated by CB[7].** For experiments on the formation of aggregates in a bulk aqueous environment, the stock solutions of NCs of **1** and CB[7] in water were mixed together in a variety of ratios (the final concentration of **1** NCs was 10  $\mu$ M) and the formation of precipitates was monitored in time. For example, in a model experiment (Supplementary Fig. 4), 1:CB[7] aggregates were prepared by the addition of 0.5 ml CB[7] solution in water (5 mM) to 2 ml of the solution of **1** NCs in water (12.5  $\mu$ M; 100 CB[7] molecules per unit NC of **1**;  $\chi = 100$ ). The formation of highly luminescent large aggregates visible to the naked eye was observed within several seconds after mixing of the stock solutions. After tens of seconds, highly flocculent material was deposited (Supplementary Figs. 4 and 5). Stability of the suspensions dependent on the CB7:1 ratio, namely,  $N_{\text{CB}[7]}/N_1 = \chi$  ( $0 < \chi < 50$ ), is presented in Fig. 3a. For the experiments described herein, we have chosen CB[7]; however, we note that other CB[*n*] homologues work similarly.

**Kinetics of 1:CB[7] formation by DLS.** For the kinetic experiments on the formation of 1:CB[7] aggregates in a bulk aqueous environment, the stock solution of **1** NCs and CB[7] in water were mixed together in a variety of ratios (the final concentration of **1** was 2  $\mu$ M), and the formation of aggregates was monitored in real time by DLS. The experimental data and their fits calculated for an Ostwald ripening model are presented in Figs. 3b and Supplementary Fig. 12. The evolution of aggregates was monitored for 24 h. We note that the aggregation processes expressed by changes in the measured hydrodynamic diameter can be an effect of complex processes involving not only the evolution of size but also changes in the shape of emerging clusters. For the selected systems, aliquots were taken for the preparation of TEM samples. The TEM images are presented in Fig. 3e and Supplementary Fig. 13.

**Composition of 1:CB[7] system.** The maximum capacity of **1** NCs towards CB[7] is described by a series of <sup>1</sup>H NMR experiments. For example, in the standard experiment, to several suspensions of **1** in D<sub>2</sub>O (containing 0.4, 0.8, 1.6, 3.2, 6.4 and 12.8 nmol of NCs in 1 ml solvent), CB[7] solution in D<sub>2</sub>O was added (1 ml; 1 mM; 1  $\mu$ mol), inducing fast precipitation of the 1:CB[7] product. The suspension was centrifuged, the supernatant was discarded and 1:CB[7] was washed with D<sub>2</sub>O four times to remove excess unbound CB[7] and MPA ligands. To the collected solids, 10  $\mu$ l DCl (20 v/v% in D<sub>2</sub>O) was added to dissolve NCs of **1** and release surface-bound CB[7] and 3-MPA species. The ratio of 1:CB[7]:MPA was calculated by comparing the integration of their signals in <sup>1</sup>H NMR (D<sub>2</sub>O) to an internal standard (pyridine; 1.0  $\mu$ mol), as shown in Supplementary Fig. 7b. The collected solids, 1:CB[7], consist of NCs of **1** with CB[7] and 3-MPA in an approximate ratio of 1<sub>1</sub>:20<sub>CB[7]</sub>:40<sub>3-MPA</sub>, which is in agreement with the FTIR spectroscopy (Supplementary Fig. 9) and elemental analysis data. Notably, the ratio of 1<sub>1</sub>:20<sub>CB[7]</sub>:40<sub>3-MPA</sub> is independent of the number of **1** NCs provided to the CB[7] solution (Supplementary Fig. 8) and consistent with the empirically found minimum amount of CB[7] required to induce the precipitation of 1:CB[7] systems ( $\chi = 18$ ; Fig. 3a). Further details are provided in the Supplementary Information.

**Real-time UV-vis experiments.** For real-time UV-vis experiments, each sample was held in a polystyrene cuvette (1.6 ml polystyrene micro-cuvette, Fisher Scientific, FB55146). Then, 7.8  $\mu$ l CB[7] (0.15 mM) solution was mixed with 600  $\mu$ l of 60 nm AuNC suspension (2.6  $\times 10^{10}$  particles per millilitre) inside the cuvette. After various amounts of time of aggregation, 16.6  $\mu$ l of the water suspension of **1** (6.2 nM to 1.2  $\mu$ M) was added. Broadband light (LS-1-LL Ocean Optics tungsten halogen lamp) was guided through a multimode fibre (numerical aperture, 0.22) and expanded by a lens before travelling through the polystyrene micro-cuvette. The transmitted light was collected by an Ocean Optics QE65000 spectrometer. The UV-vis spectra were recorded in real time with 40 ms integration time and 1 s delay time.

**Studies on kinetic entrapment of colloidal stable plasmonic aggregates.** In a typical experiment, the aggregation of **2b** AuNCs (60 nm; BBI Solutions) was first triggered by mixing 1–3  $\mu$ l CB[*n*] solution (1 mM) and 3 ml of the AuNCs suspension in a quartz cuvette. After a certain amount of time of CB[*n*]-mediated aggregation (typically between 0 and 20 min), an aqueous suspension of **1** NCs (5  $\mu$ M;  $\chi = 5$ –10) was added to quench the assembly and stabilize the aggregates. Number ratio between **1** and **2b**, namely,  $n_1/n_{2b} = 10^4$ , is used to ensure that the **2b** interfaces are covered by **1** NCs. Morphology of the **2b**:CB[*n*]:**1** hybrids is determined by the structure of central plasmonic component whose growth is kinetically arrested by the addition of **1** NCs. Kinetically arrested states are typically less uniform in comparison to thermodynamically controlled structures. However, here the reported processes allow for the facile and effective stabilization of optical properties of the plasmonic component while providing outstanding colloidal stability and structure permeability for photochemistry. We note that control over the optical properties and colloidal stability is also demonstrated for 5 nm and 12 nm AuNCs (Supplementary Figs. 23 and 24). Further details are available in the Supplementary Information.

**Tracking light-driven out-of-equilibrium redox chemistry.** Sample preparation. All the SERS tracking experiments were conducted in an inert atmosphere. Citrate-coated colloidal **2b** AuNCs (60 nm; BBI Solutions) and deionized water were deoxygenated using the freeze-pump-thaw degassing procedure and Schlenk line technique. Self-assembly of hybrid **2b**:CB[*n*]:**1** aggregates in an aqueous environment was carried out in a wet glovebox with a dioxygen level of <0.1 ppm. In a typical experiment, CB[*n*]-bridged AuNC aggregation was first triggered by mixing the CB[*n*] solution and 3 ml AuNC suspension in a quartz cuvette (Hellma Analytics, 111-QS, 10  $\times$  10  $\times$  35 mm). After 5 min of CB[*n*]-mediated aggregation, an aqueous suspension of **1** NCs was added to quench the assembly and stabilize the aggregates. To yield optimal SERS with the 785 nm excitation laser, the aggregation was selectively quenched at the point where the aggregates have strong resonance at 785 nm ( $\text{Abs}_{785 \text{ nm}} = 0.6$ ). This was further followed by the addition of a dimethyl viologen solution to give  $N_1:N_{\text{CB}[n]}:N_{\text{MV}^{2+}}$  ratio = 1:5:5, ensuring that all the MV<sup>2+</sup> species are chemisorbed within the aggregates. The cuvette was tightly sealed to prevent O<sub>2</sub> contamination and used in further in situ SERS experiments. Operando SERS experiments. Raman spectroscopy was performed on a Renishaw Via Raman microscope. Stable suspensions of **2b**:CB[7]:**1** C MV<sup>2+</sup> were uniformly illuminated with molecular off-resonance excitation at 302 nm wavelength (pump light) and in situ SERS was realized using a 785 nm diode laser (probe light; Supplementary Fig. 41). The diode laser (785 nm) was focused on the interface of the aggregate suspension through the quartz cuvette wall with  $\times 5$  objective (numerical aperture, 0.12). The depth of suspension along the light path was 10 mm. Raman scattering was collected using the same objective and analysed using a grating of 1,200 lines per millimetre and a charge-coupled device camera. Spectra were collected with 5 s integration time and the laser power on the sample was 125 mW.

**DFT calculations.** We performed DFT calculations using the dispersion corrected hybrid functional  $\omega$ B97X-D<sup>47</sup> with an implicit solvation model<sup>48</sup> (parametrized for

water). Geometry optimizations were performed with the 6-311G(d,p) triple-zeta basis set with polarization functions. Vibrational analysis was done at the same computational level to ensure that the optimizations resulted in local minima, to calculate thermal and entropic corrections, and to obtain the Raman spectra. For every system, the highest occupied molecular orbital and lowest unoccupied molecular orbital were mixed for the initial guess for the DFT wavefunction, and its stability was analysed and optimized, if needed. To ensure high accuracy, electronic energies were recalculated at the  $\omega$ B97X-D/6-311++G(3df,3pd) level of theory. As the thermodynamic data given by the Gaussian09 (rev E.01) software<sup>49</sup> were calculated for  $T=298.15$  K and  $p=1$  atm, concentration correction was applied:  $\Delta G_{\text{conc}} = RT \ln(24.465c)$ , where  $c$  is the concentration of the calculated compound (in  $\text{mol dm}^{-3}$ ),  $R$  is the universal gas constant,  $T$  is the temperature and  $p$  is the partial pressure. For the different redox states of methyl viologen,  $c=1.0$   $\text{mol dm}^{-3}$  was applied, but for the  $\pi$ -dimer and  $\sigma$ -dimer states,  $c=0.5$   $\text{mol dm}^{-3}$  concentration was considered. The presented free energy values are calculated by applying the corrections on the electronic energy obtained at the  $\omega$ B97X-D/6-311++G(3df,3pd) level of theory. Further details on calculations are available in the Supplementary Information, including discussion on (1) redox states of methyl viologen; (2) assembly processes of methyl viologen species on a different redox state (that is, formation of  $\pi$ -(MV<sup>+</sup>)<sub>2</sub> dimers, [MV<sup>2+</sup>:MV<sup>0</sup>] heterobinary complexes and  $\sigma$ -(MV<sup>+</sup>)<sub>2</sub> dimeric species); and (3) host-guest interactions of viologen species with CB[ $n$ ] species. Computational spectra were scaled by a factor to match with the experiment. Further details on matching are available in the Supplementary Information.

### Data availability

Methods and materials characterization are provided in the Supplementary Information. The data that support the findings of this study are available from the corresponding author on reasonable request.

### References

- Kim, J. et al. New cucurbituril homologues: syntheses, isolation, characterization and X-ray crystal structures of cucurbit[ $n$ ]uril ( $n=5, 7$ , and  $8$ ). *J. Am. Chem. Soc.* **122**, 540–541 (2000).
- Xie, R., Battaglia, D. & Peng, X. Colloidal InP nanocrystals as efficient emitters covering blue to near-infrared. *J. Am. Chem. Soc.* **129**, 15432–15433 (2007).
- Kimling, J. et al. Turkevich method for gold nanoparticle synthesis revisited. *J. Phys. Chem. B* **110**, 15700–15707 (2006).
- Chai, J.-D. & Head-Gordon, M. Long-range corrected hybrid density functionals with damped atom-atom dispersion corrections. *Phys. Chem. Chem. Phys.* **10**, 6615–6620 (2008).
- Marenich, A. V., Cramer, C. J. & Truhlar, D. G. Universal solvation model based on solute electron density and on a continuum model of the solvent defined by the bulk dielectric constant and atomic surface tensions. *J. Phys. Chem. B* **113**, 6378–6396 (2009).
- Frisch, M. J. et al. Gaussian09 revision E.01 (Gaussian Inc., 2009).

### Acknowledgements

We acknowledge financial support from EPSRC grant nos. EP/L027151/1 (NoTCH) and EP/R020965/1 (RaNT). J.H. is thankful for support from the Chinese Scholarship Council and Cambridge Commonwealth, European and International Trust. B.d.N. acknowledges support from the Leverhulme Trust and Isaac Newton Trust. R.C. acknowledges support from Trinity College, Cambridge. S.M.C. thanks Girton College, Cambridge, for a Henslow Research Fellowship. We thank S. J. Barrow, A. S. Groombridge and I. Szabó for helpful discussions. We acknowledge use of the research computing facility at King's College London, Rosalind (<https://rosalind.kcl.ac.uk>).

### Author contributions

K.S. and O.A.S. conceived the project and developed the experiments. K.S. developed and prepared the materials. K.S. and J.A.M. carried out the mechanistic studies on self-limiting aggregation. K.S. and O.A.S. proposed the aggregation mechanism. D.D.X. carried out the zeta potential measurements. K.S. and J.H. carried out SERS experiments. K.S., J.H., B.d.N. and J.J.B. analysed the SERS data while K.S. and O.A.S. provided interpretation and proposed a mechanism for the photochemical transformations. T.F. and E.R. carried out the theoretical calculations. K.S. and S.M.C. carried out TEM experiments. R.C. carried out calculations on the optical properties of AuNC aggregates while R.C., J.H., B.d.N. and J.J.B. provided their interpretation. K.S., J.A.M. and O.A.S. analysed the data and wrote the manuscript with input from all co-authors.

### Competing interests

The authors declare no competing interests.

### Additional information

**Supplementary information** The online version contains supplementary material available at <https://doi.org/10.1038/s41565-021-00949-6>.

**Correspondence and requests for materials** should be addressed to O.A.S.

**Peer review information** *Nature Nanotechnology* thanks Hongyu Chen, Zhihong Nie and the other, anonymous, reviewer(s) for their contribution to the peer review of this work.

**Reprints and permissions information** is available at [www.nature.com/reprints](http://www.nature.com/reprints).